NJC

ROYAL SOCIETY OF CHEMISTRY

PAPER

View Article Online
View Journal | View Issue

Cite this: *New J. Chem.*, 2024, **48**, 13492

Enhancement of the electrochemical properties of vanadium dioxide *via* nitrogen-doped reduced graphene oxide for high-performance supercapacitor applications†

Samba Sarr, [a] Daba T. Bakhoum,[a] Ndeye F. Sylla,[a] Ndeye M. Ndiaye,[b] Delvina J. Tarimo, [a] Vusani M. Maphiri,[a] Balla D. Ngom[b] and Ncholu Manyala *[a]

Received 4th March 2024,
Accepted 2nd July 2024

DOI: 10.1039/d4nj01029a

rsc.li/njc

A one-step solvothermal approach was used to integrate nitrogen-doped reduced graphene oxide into vanadium dioxide (VO_2) to prepare a V@*X*N-G (where *X* = 24, 48 and 96 and is the mass of urea as the nitrogen (N) source) nanocomposite material. After optimization, V@48N-G showed better performance with a specific capacitance of 197.4 F g^{-1} at 0.5 A g^{-1} in a wide working potential window of 0.0–0.8 V *vs.* silver/silver chloride and was adopted as a positive electrode. Thus, cocoa waste-based activated carbon (ACC) was investigated and considered a negative electrode in assembling an asymmetric full-cell V@48N-G//ACC. The device exhibited good specific energy and power of 28.8 W h kg^{-1} and 425.1 W kg^{-1}, respectively, at a voltage window and specific current of 1.7 V and 0.5 A g^{-1}, respectively. Its cycling stability resulted in a Coulombic efficiency (CE) and capacitance retention (CR) of 99.8% and 73%, respectively, over 10 000 galvanostatic charge/discharge cycles at 10 A g^{-1}. Therefore, the V@48N-G//ACC device shows excellent electrochemical performance and is suitable for energy storage application technology.

1. Introduction

The depletion of fossil fuels has motivated and accelerated intensive research to produce, convert and store energy efficiently, adequately and sustainably to secure socio-economic development.[1,2] Renewable energy sources such as wind and sun drive the need for superior and sustainable energy technologies.[3] For the efficient utilization of these energy sources, appropriate energy storage systems such as flywheels, batteries and supercapacitors are required to store excess generated energy and release the energy when low or no energy is being generated. Supercapacitor (SC) energy storage systems have attracted significant attention owing to their low maintenance, great specific power, rapid charge propagation dynamics and very long cycling life performance (up to 100 000 cycles).[4–7]. In addition to its impressive specific power of 10^3 W kg^{-1}, which is thousands of times greater than batteries (50–200 W kg^{-1}), supercapacitors also have a specific energy of around of ~5–10 W h kg^{-1}. This specific energy is significantly more than that of electrostatic capacitors (<1 W h kg^{-1}), but still lower than that of batteries.[5,8,9] Thus, prodigious research efforts are being developed to improve the specific energy of supercapacitors to match that of batteries. This can be possible by optimising the performance of electrode materials since they play a key role in the overall device performance. Therefore, the study of materials with distinct properties has gained great interest in supercapacitor applications.

Transition metal oxides (TMOs) with multiple oxidation states produce higher specific capacitances (C_{sp}) than conducting polymers and carbonaceous materials.[10] TMOs, such as ruthenium dioxide (RuO_2), cobalt oxide (Co_3O_4), manganese dioxide (MnO_2), nickel oxide (NiO), and vanadium oxide (VO_x), are typical electrode materials for supercapacitor applications and thus have been used as Faradaic/pseudocapacitor electrode materials.[11–14] Particularly, vanadium dioxide (VO_2) has attracted enormous interest owing to its several oxidation states (2+, 3+, 4+ and 5+), low cost, low toxicity, optoelectronic properties and unique electronic structure. VO_2 has been widely used as an electrode material in energy storage applications.[15,16] However, owing to its low electrical conductivity, slow ion diffusion and poor cycling stability, its practical application is limited.[10,17,18]

An effective technique to overcome this drawback of VO_2 electrodes as other TMOs is through incorporating carbon materials (in other words, electrical double layer capacitors

[a] *Department of Physics, Institute of Applied Materials, SARChI Chair in Carbon Technology and Materials, University of Pretoria, Pretoria 0028, South Africa. E-mail: ncholu.manyala@up.ac.za*

[b] *Laboratoire de Photonique Quantique, d'Energie et de Nano-Fabrication, Faculté des Sciences et Techniques, Université Cheikh Anta Diop de Dakar (UCAD), B.P. 5005, Dakar-Fann Dakar, Senegal*

† Electronic supplementary information (ESI) available. See DOI: https://doi.org/10.1039/d4nj01029a

(EDLCs) nanomaterials) like carbon aerogels, activated carbon, carbon nanotubes and reduced graphene oxide to make a composite material. This can improve some TMOs properties including the electrical conductivity, cycling stability, and ion diffusion.[19,20] For example, Liang *et al.*[21] reported a coaxial-structured material based on CNTs enveloped by a few layers of VO_2(B) sheath (VO_2(B)/CNTs) by the controlled hydrolysis of vanadium triisopropoxide *in situ*. The composite VO_2(B)/CNTs demonstrated a superior specific capacitance and better rate capability than the single component, showing 250 F g^{-1} as the specific capacitance in 1 M sodium sulphate neutral electrolyte at a specific current of 0.5 A g^{-1} and a CR of 71% at 10 A g^{-1}.[21] Xiao and co-workers[22] reported VO_2(B) nanobelts regularly embedded into the nanosheets of graphene by the hydrothermal method, in which GO was reduced to reduced graphene oxide (rGO). The VO_2(B)/rGO composite electrode exhibited a mass capacitance value of 290.4 F g^{-1} linked to 209.2 F g^{-1} for the pure VO_2(B) at 0.2 A g^{-1} in 1 M Na_2SO_4.[22] Dhanda and colleagues[23] synthesized VO_2/g-C_3N_4 composites employing the hydrothermal method. The optimised 3VO_2/g-C_3N_4 sample showed a specific capacitance value of 1416 F g^{-1} compared to 583.3 F g^{-1} for VO_2(D) at a sweep rate of 2 mV s^{-1} in 1 M potassium hydroxide electrolyte.[23] These studies concluded that the composite material performs better than pure VO_2. These good electrochemical performances are ascribed to the synergistic outcome, which improves the electron transfer originated from the carbon-based material and charge storage capacities/capacitances due to VO_2.[24] On the other hand, carbon materials have the disadvantage of having a low specific capacitance. Therefore, in order to optimize the performances of composite materials, it is of interest to improve the EDLC materials performances and thus build a composite material. In particular, single-layer rGOs attract each other owing to the van der Waals force, resulting in the restacking of the material (rGO). This restacking reduces the surface area and then less capacitance is stored throughout the development of the double layer.[25] Thus, the most universally appropriate strategy to enhance the specific capacitance for EDLC materials is the introduction of a spacer material or heteroatom doping.

Heteroatom doping such as sulphur (S), boron (B), oxygen (O) and nitrogen (N) can improve the capacitance properties of rGO by preventing the restacking by increasing the interlayer spacing. Moreover, doping with heteroatom increases the electronic conductivity of rGO.[26] Consequently, the combined benefits amongst the pseudocapacitor (PC) material and the EDLC material doped with heteroatoms will provide excellent specific capacitance, interesting cycling properties, and high rate capability for the hybrid composite, showing great supercapacitive performances.[27]

Herein, we have established a low cost-effective, environment-friendly approach to enhance the electrochemical properties of vanadium dioxide (VO_2) by the incorporation of N-doped reduced GO using a simple solvothermal process. The prepared material was characterized using different techniques such as X-ray diffraction (XRD) spectroscopy, Raman spectroscopy, Fourier transform infrared (FTIR) spectroscopy, energy dispersive X-ray (EDX) spectroscopy, field emission scanning electron microscopy (FESEM) and N_2-adsorption/desorption isotherms together with the equivalent pore size distribution. The optimized composite (V@48N-G) was investigated in both three and two-electrodes configuration. In the two-electrode configuration, the assembled device combined V@48N-G and cocoa waste-based activated carbon (ACC) as the positive electrode and negative electrode, respectively, with a high specific energy of 28.8 W h kg^{-1}. Thus, the prepared material is a suitable candidate for energy storage applications.

2. Experimental

2.1. Material synthesis

The materials utilized in this work were prepared similarly as those in our previous works.[28,29] Vanadium dioxide nitrogen-doped reduced graphene oxide nanocomposites were produced using the solvothermal technique, where VO_2 and reduced graphene oxide were prepared, as detailed in the ref 28 and 30. In summary, vanadium pentoxide (V_2O_5) was mixed with oxalic acid dihydrate ($C_2H_2O_4{\cdot}2H_2O$) at a mass ratio of 1.2 : 3.6 g, respectively, under continuous stirring at a constant heat of 80 °C for 3 h till a uniform dark blue (vanadyl oxalate (VOC_2O_4)) solution was formed. Thereafter, nitrogen-doped reduced graphene oxide was prepared by dispersing 16 mg of reduced graphene oxide and different *X* amounts of urea in a volume of 10 mL deionized water (DW), then sonicated for 150 min. The obtained solution was labeled *X*N-G, where *X* = 24, 48 and 96 mg of urea as the nitrogen (N) source and G represent the reduced graphene oxide. Note that reduced graphene oxide was optimized in our previous work,[29] exhibiting that the best amount of reduced graphene oxide added was 16 mg. 6 mL of VOC_2O_4 solution was mixed with 60 mL of isopropanol, then subsequently transferred into the *X*N-G mixture. The obtained solution was then homogenized by stirring for 20 min at a constant heat of 80 °C, shifted into a Teflon-lined autoclave and retained in an oven for 6 h at 200 °C. The autoclave was then allowed to naturally cool down to ambient conditions before collecting and thoroughly cleaning the products with DW and ethanol *via* centrifugal agitation and decantation of the liquid. After drying overnight in an electric oven at 60 °C, the obtained samples were named as V@24N-G, V@48N-G, and V@96N-G, where V represents vanadium dioxide. Scheme 1 shows different V@*X*N-G composite preparation stages.

2.2. Material characterization

The structure of VO_2 and V@*X*N-G composite materials was obtained by the aid of a Bruker BV 2D PHASER Benchtop powder X-ray diffraction instrument (PANalytical BV, Amsterdam, Netherland) operated with a Cu Kα_1 (λ = 0.154056 nm) radiation source. The unit cell of the obtained VO_2 structure was visualized using Vesta software and the corresponding crystallographic information file (CIF). A WITec alpha 300 RAS+ confocal micro-Raman microscope (Ulm, Germany) at a laser wavelength and power of 532 nm and 3.41 mW, respectively, and a spectral

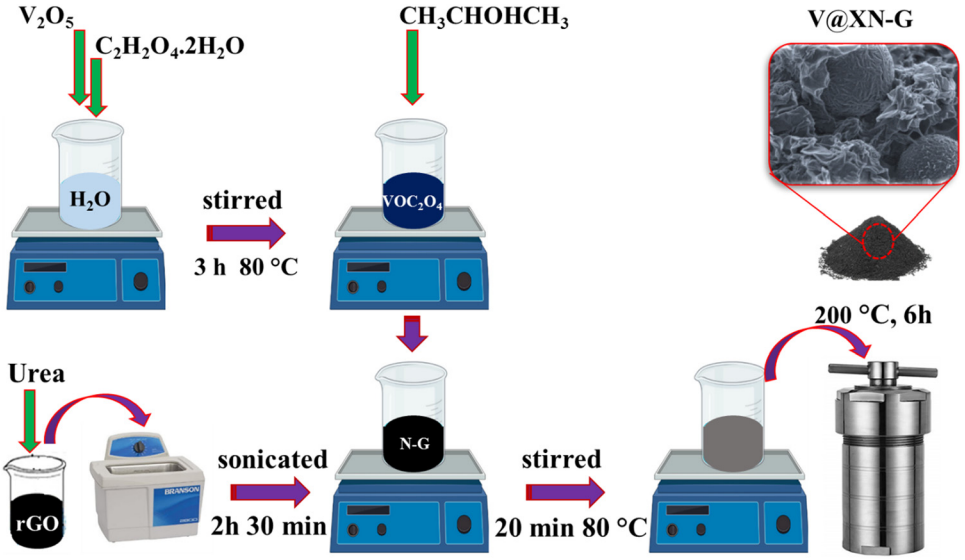

Scheme 1 Illustration of the V@*X*N-G composite synthesis process.

acquisition time of 60 s together with a Bruker Alpha-platinum-Attenuated Total Reflectance (Billerica, MA, USA) was used to perform Fourier transform infrared (FTIR) spectroscopy at 32 scans to analyse the diverse vibrations of the prepared materials. Quantachrome (NOVAtouch NT 2 LX-1, 220 V, USA) equipment was employed to analyze the specific surface area (SSA) alongside the pore size distribution (PSD) of the samples using the Brunauer–Emmett–Teller (BET) and density functional theory (DFT) techniques in the range of 0.05–0.95 relative pressure (P/P_0) at 77 K. The samples micrographs followed by the energy dispersive X-ray (EDX) spectra were investigated using a Zeiss Ultra Plus 55 field emission scanning electron microscope (FE-SEM; Akishima-shi, Japan) coupled with an Oxford EDX operated at 2.0 and 20 kV accelerating potential, respectively. X-ray photoelectron spectroscopy (XPS) measurements were conducted with a VG Escalab 220i-XL instrument equipped with a monochromatic Al–K excited energy source (0.6 eV) and a hemispherical electron energy analyzer with an angle of 180°.

2.3. Electrochemical characterization

In this study, the electrodes used were fabricated by mixing the as-prepared samples as active materials, acetylene carbon black (ACB) as the conductive additive and polyvinylidene difluoride ($-(C_2H_2F_2)_n-$, PVDF) as a binder in a mass ratio (in percentage) of 80 : 10 : 10, respectively, in an agate mortar with the dropwise addition of *N*-methyl pyrrolidone (NMP) to make a homogenous slurry. The resulting slurry was then pasted onto rectangular (1 × 2 cm^2) and circular (1.8 cm^2) clean nickel foam adopted as a current collector to fabricate electrodes for three and two-electrode measurements. The electrodes were then dried at 60 °C in an electric oven for 12 h. Afterwards, the supercapacitor performances of the fabricated electrodes were obtained using a Bio-Logic VMP-300 potentiostat (Knoxville, TN, USA) accompanied by the EC-Lab V11.33 software (Edmonton, AB, Canada) by means of the three and two-electrode configurations. The three-electrode test was done utilizing a glassy carbon as the counter electrode, silver/silver chloride (Ag/AgCl) as the reference electrode and the prepared samples representing the working electrode, while the two-electrode set-up was used to assemble an asymmetric device, in which a microfiber filter paper was used as a separator to sandwich between V@*X*N-G and ACC as the positive and negative electrodes, respectively, in a Swagelok cell. All the electrochemical tests, *i.e.*, cyclic voltammetry (CV), galvanostatic charge/discharge (GCD) and electrochemical impedance spectroscopy (EIS), were performed in the range from 100 kHz to 10 mHz at room temperature using 0.5 M K_2SO_4 neutral electrolyte.

3. Results and discussion

3.1. Structural, morphological, and textural analysis

Fig. 1(a) depicts the powder X-ray diffraction (XRD) patterns of VO_2 and V@*X*N-G composite samples. The patterns were indexed to the inorganic crystal structure database (ICSD) of VO_2 (A) (card #1503)[28] and to the peaks for the (002) and (100) planes of rGO material. The XRD pattern shows the co-existence of VO_2 and rGO in all the three composite materials, confirming the good incorporation of rGO into the VO_2 material.[31]

The V@*X*N-G composites were further examined with Raman spectroscopy, as shown in Fig. 1(b), confirming the existence of VO_2 through its different vibrational modes, as previously revealed in our work.[28] Thus, V–O–V bending and stretching and V=O stretching modes are attributed to the Raman shift range from 100 to 400 cm^{-1} and 400 to 800 cm^{-1}, and ~997 cm^{-1}, respectively.[28,32] Additionally, the Raman spectra show two strong characteristic bands attributed to the defects (D) and graphitic (G) bands caused by the defects (disordered) of the edges of graphite and graphene materials and the tangential vibration of the sp^2 carbon atoms as a result of the highly ordered hexagonal structure within the graphite, respectively. These typical bands of carbon nanostructure demonstrate the existence of graphene in all the

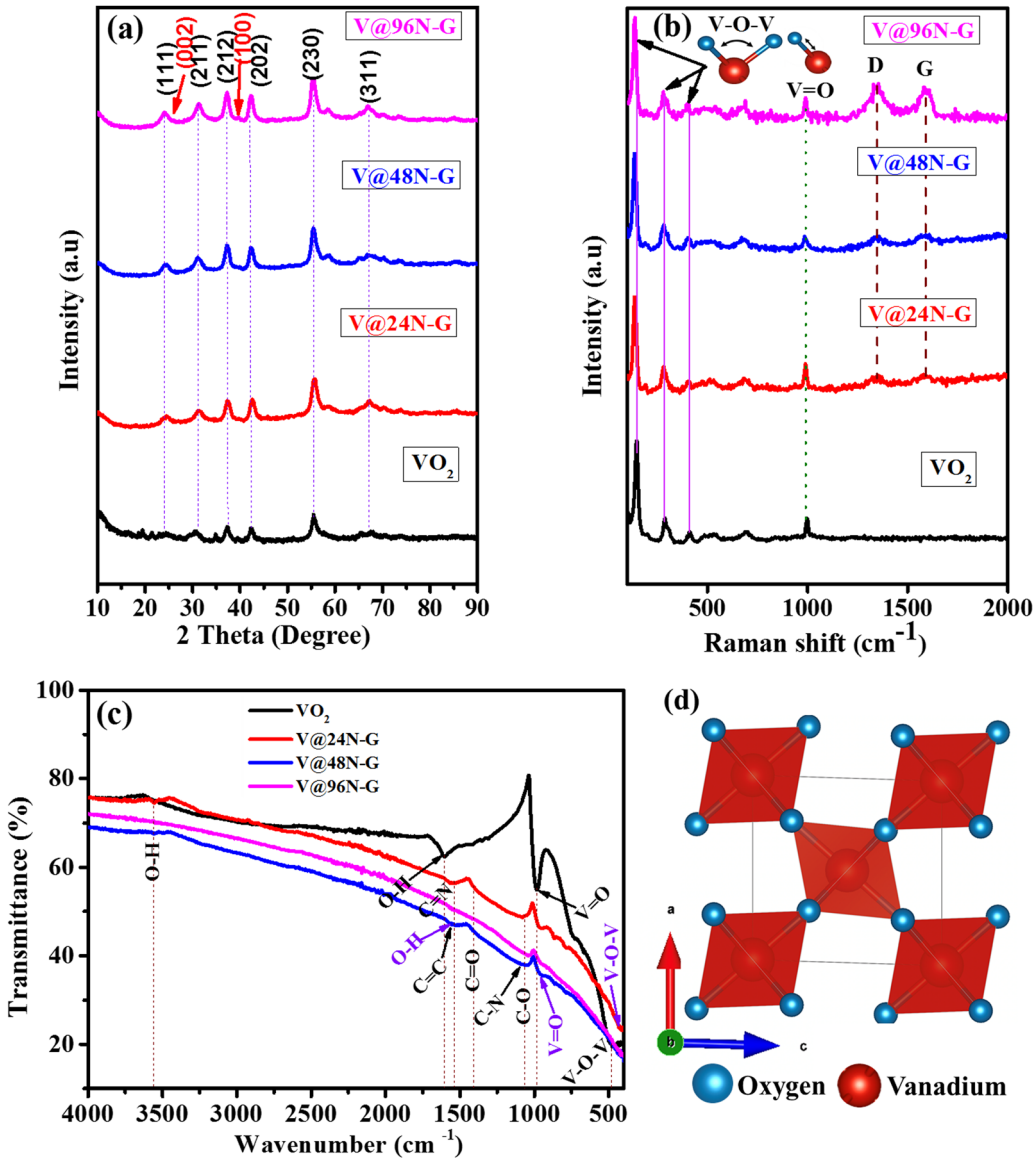

Fig. 1 (a) XRD, (b) Raman, (c) FTIR patterns of VO_2 and V@*X*N-G nanocomposites, and (d) the unit cell of VO_2.

prepared nanocomposite materials.[33,34] Consequently, the Raman results confirm the presence of carbon peaks revealed by the XRD analysis.

The intensity ratio (I_D/I_G) of the D and G-bands for the V@*X*N-G composite was investigated to estimate the degree of graphitization of the carbon materials.[35] The calculated values of the I_D/I_G ratio together with the D and G-bands peak position are presented in Table 1. Note that the I_D/I_G ratio increases as the nitrogen content incorporated into the rGO increases. This can be explained through the interruption of the symmetry of the lattice caused by the introduction of the heteroatom into the graphitic structure. Therefore, the incorporation of N into the carbon lattice produces distortions, which transform the graphitic site (sp^2) into the sp^3 domain.[35–37]

Fourier transform infrared spectroscopy (FTIR) measurements of pristine VO_2 and V@*X*N-G were studied to investigate

Table 1 Peak position of the vibrational Raman D- and G-bands with intensity ratio I_D/I_G, and textural properties of VO_2 and V@*X*N-G composites

Samples	D-band position (cm^{-1})	G-band position (cm^{-1})	Intensity ratio (I_D/I_G)	BET SSA ($m^2\ g^{-1}$)	Total pore volume ($cm^3\ g^{-1}$)	Average pore size (nm)
VO_2	—	—	—	24.23	0.085	13.05
V@24N-G	1353	1579	0.98	20.43	0.055	11.47
V@48N-G	1357	1606	0.99	9.44	0.028	12.61
V@96N-G	1357	1583	1.01	7.37	0.024	12.62

the chemical bonds between oxygen, vanadium, nitrogen and carbon atoms in the synthesized nanostructures. As exposed in Fig. 1(c), the peaks at about 983 and 478 cm^{-1} are assigned to the stretching vibration modes of V═O and V–O–V, respectively.[38,39] The peak at about 1606.7 cm^{-1} indicates the in-plane bending vibration mode of O–H while the peak at 3553.6 cm^{-1} is assigned to the O–H stretching vibration mode.[40] These vibration bands identified for the pristine VO_2 exist in the composite V@*X*N-G as well. However, a decrease in the intensity with a small shifting towards the lower wavenumbers is noted for these peaks such as O–H (1606.7–1565 cm^{-1}), V═O (983–961 cm^{-1}), and V–O–V (478–431 cm^{-1}). This is due to the interaction between VO_2 and the *X*N-G. Furthermore, some additional peaks appear in the composites. Thus, the peak positioned at about 1407 cm^{-1} is ascribed to the C═O vibration mode, while that at about 1066 cm^{-1} is associated with C–O stretching.[41,42] Two absorption peaks at about 1540 cm^{-1} and 1066 cm^{-1} are observed as expected, which correspond to the typical absorption bands of C═N and C–N, respectively, indicating the presence of nitrogen in the composites.[43] An absorption band appears at about 1571 cm^{-1}, partially overlapped with C═N, corresponding to the aromatic skeletal C═C vibrations.[41] These results support the successful composite preparation *via* the solvothermal approach.

The unit cell of the VO_2 structure is displayed in Fig. 1(d). In summary, the VO_2 monoclinic crystal structure is visualized, in which the vanadium atoms occupy an octahedral coordination site. It can be seen that the vanadium atom lies at the centre surrounded by six oxygen atoms.[44] The vibration modes are shown as the inset in the Raman spectrum (Fig. 1b).

The textural properties of VO_2 and V@*X*N-G were analyzed through nitrogen sorption isotherms and PSD curves, as shown in Fig. 2. The isothermal analysis reveals type IV features associated with a H3 hysteresis loop for all the composites (V@24N-G, V@48N-G, and V@96N-G), suggesting the mesoporous structure of the samples, as shown in Fig. 2a.[45,46] The pore size distribution curves of the samples (Fig. 2b) were recorded in the 2–16 nm pore diameter range, confirming the presence of a mesoporous structure, as also observed in the isotherms (Fig. 2a). The textural properties of the synthesized materials are displayed on Table 1. The pristine material (VO_2) gives a higher specific surface area (SSA) and total pore volume than the composites (V@*X*N-G). It can be elicited that the introduction of *X*N-G into the VO_2 sample decreases the SSA and total pore volume. This decrease is proportional to the amount of nitrogen added into the rGO matrix. Therefore, the high amount of nitrogen reduces the SSA by blocking some pores of the material.[47] However, it is noted that the composite materials perform better as the electrode for supercapacitor applications.

The morphology analysis of the composites (V@24N-G, V@48N-G and V@96N-G) materials is presented in Fig. 3 obtained by a field emission scanning electron microscope (FESEM). The FESEM micrograph of pristine VO_2 revealed microspheres-like morphology assembled with nanograins on their surface (Fig. S1, ESI†).[28] Fig. 3(a)–(f) exhibit a similar morphology at low and high magnification for all the composites, showing a network of the VO_2 morphology and an interconnected nanosheets-like structure of N-G.[48,49] The SEM images demonstrate an embellishment of N-G nanosheets on the surface of the microspheres. In particular, Fig. 3(c) and (d) show a good incorporation of VO_2 in the N-G sheets, demonstrating a great interaction between VO_2 microspheres and N-G. This can provide better electrochemical performance due to the good synergistic effect.

Energy dispersive X-ray (EDX) spectroscopy was also investigated to carry out the elemental composition of the as-synthesized composites materials. Fig. 4 displays the EDX spectra of V@24N-G, V@48N-G and V@96N-G composite materials.

It was observed that the synthesized composites contain the expected elements C, V, N and O. The insets in Fig. 4(a)–(c) display a description of the weight percent composition of each element.

The presence of sliver (Ag) and gold (Au) elements in the EDX spectra is ascribed to the Ag tape and Au conductive coat utilized in the EDX preparation. The elemental distribution mapping images confirms the good distribution of the elements (C, V, N and O) in the composites, as shown in Fig. S2 (ESI†), which confirms the fruitful integration of nitrogen into the rGO structure.

X-ray photoelectron spectroscopy (XPS) was conducted to further analyze the surface chemical property and the elemental composition of the synthesized pristine VO_2 and composite materials V@*X*N-G. Fig. 5(a) displays the survey scan of the VO_2

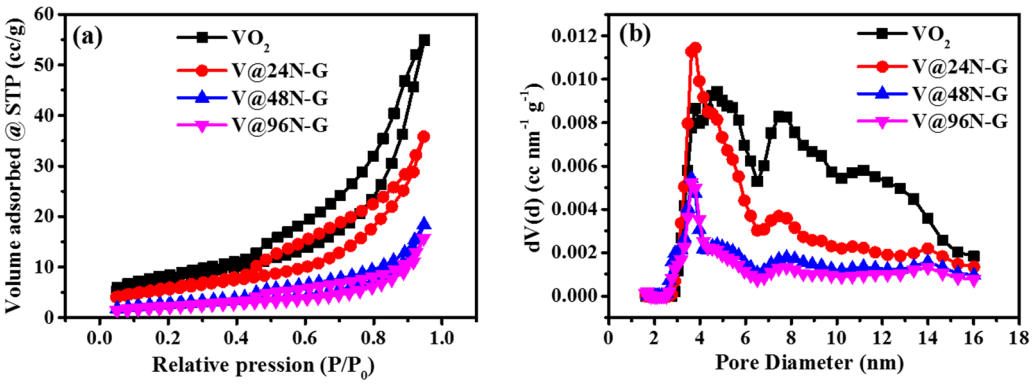

Fig. 2 (a) N_2-adsorption/desorption isotherm curves and (b) PSD curves of VO_2 and V@*X*N-G nanocomposites.

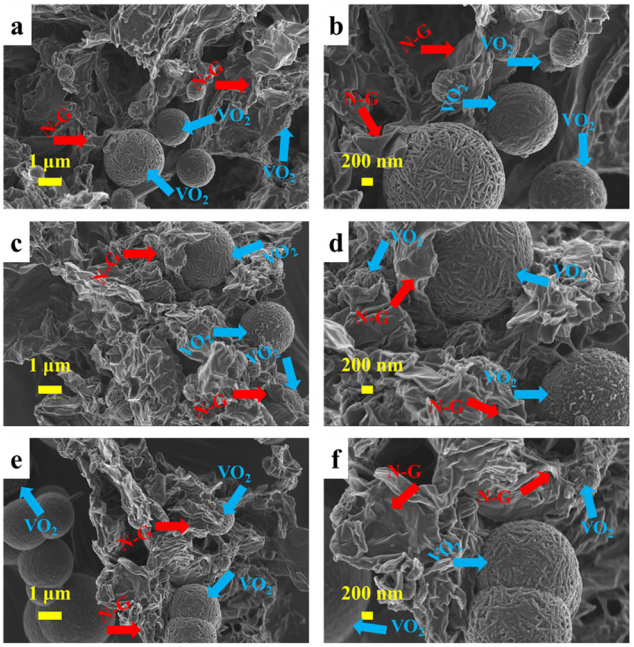

Fig. 3 FESEM images of (a) and (b) V@24N-G, (c) and (d) V@48N-G, and (e) and (f) V@96N-G at low and high magnifications.

and V@*X*N-G composite samples. Herein, the XPS analysis of the V@48N-G sample that showed better features from previously discussed characterizations is detailed. The XPS survey spectrum reflects the elemental composition of the materials, showing four characteristic peaks of V 2p at 516.5 eV, O 1s at 529.3 eV, C 1s at 284.5 eV and N 1s at 400.7 eV, as illustrated in Fig. 5(a). This is in line with the EDS elemental composition results. The appearance of the additional V_{LMN} and O_{KLL} peaks (electrons auger) confirms the presence of V and O elements in the sample.[50,51] The spectra were deconvoluted for in-depth analysis. The deconvoluted V 2p spectra has three V $2p_{3/2}$ peaks corresponding to the oxidation state of vanadium V^{3+} at 515.1 eV, V^{4+} at 516.5 eV and V^{5+} at 516.9 eV; similarly, the V $2p_{1/2}$ peak displays V^{3+} at 522.7 eV, V^{4+} at 524.0 eV and V^{5+} at 525.1 eV (Fig. 5b). The intense peaks at binding energy of 516.5 and 524.0 eV predict that V^{4+} is predominant in the material compared to V^{3+} and V^{5+}, as shown in Fig. 5(b). The presence of V^{3+} can be due to the carbothermal reduction while V^{5+} comes from the V_2O_5 precursor.[51,52] The O 1s spectra, deconvoluted in Fig. 5(b), shows the occurrence of V–O (529.1 eV), C═O (529.8 eV) and C–O/O═C–O (531.5 eV) interactions.[53,54] The deconvoluted C 1s spectra (Fig. 5c) elucidate the presence of distinct types of carbon bonds. The carbon peak at 284.5 eV can be accredited to sp^2 (C═C) or sp^3 (C–C) hybridized carbons.[50,55] The peak at about 285.2 eV is attributed to C–N, while the peak at 287.2 eV is assigned to C═O or C–O.[52,56,57] The result indicates the formation of the N-doped carbon skeleton, conforming the FTIR result. The N 1s high-resolution XPS spectrum (see Fig. 5d) can be curve-fitted into three distinct peaks at approximately 399.5, 400.8 and 402.3 eV, associated with pyridinic-N, pyrrolic-N and graphitic-N, respectively.[20,58] The high-resolution XPS results of the other samples (VO_2, V@24N-G and V@96N-G) are shown in Fig. S3 and S4 (ESI†). Table 2

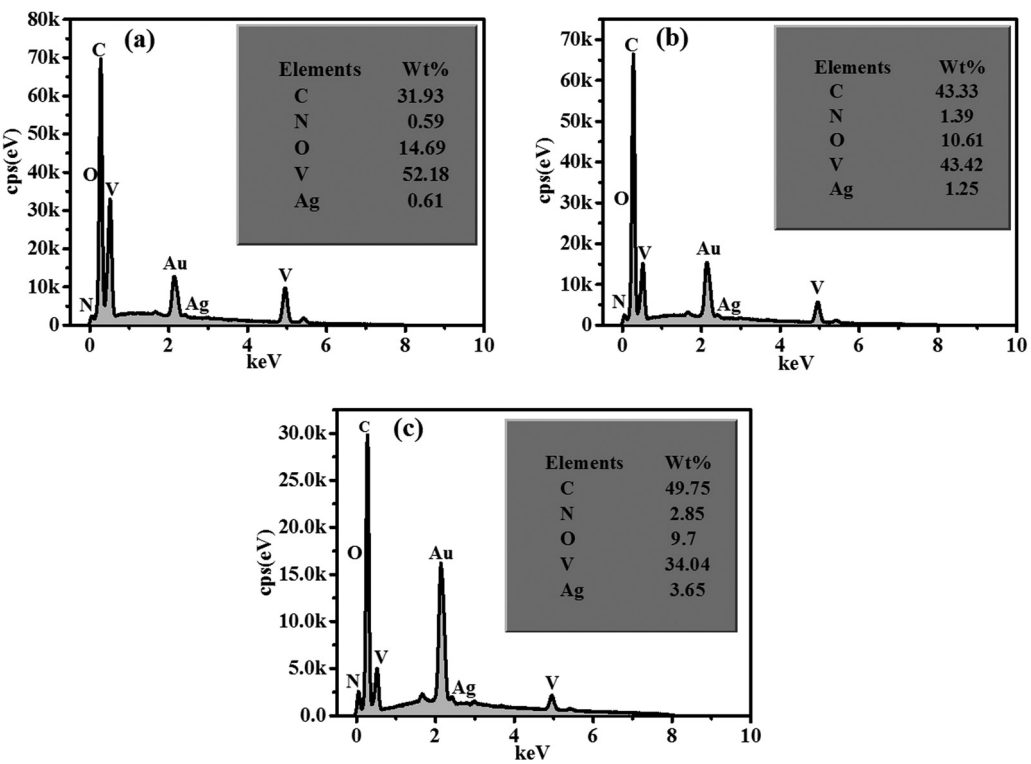

Fig. 4 EDX spectrum of (a) V@24N-G, (b) V@48N-G and (c) V@96N-G composite materials.

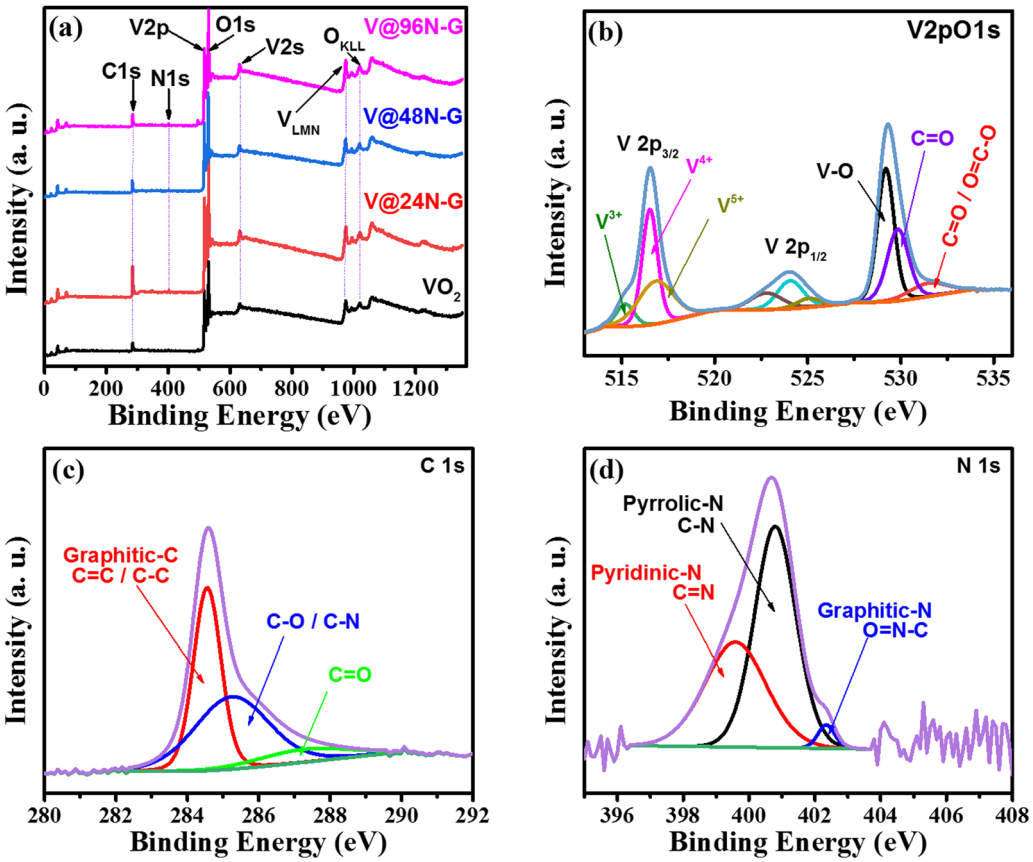

Fig. 5 XPS analysis: (a) survey scan of all the samples, (b) V 2p and O 1s, (c) C 1s and (d) high-resolution N 1s spectrum of V@48N-G.

displays the description of the atomic percent composition of each element for different samples. The N-doping provides more active sites for ion adsorption and improves the electron transferability of the carbon material; thus, electrolyte ions are more conducive to diffuse when the charging/discharging behavior occurs to increase the energy storage capabilities.[57]

Thus, the presence of pyridinic-N and pyrrolic-N favours charge storage owing to the enhanced charge accumulation at the electrode/electrolyte interface and the electrode surface wettability. Additionally, graphitic-N and pyridinic-N enhance electron transport, thus improving the electrical conductivity of the electrode materials.[55,59] The various nitrogen functional groups may improve the electrochemical performance of the material.

As shown in Table 2, the wide scan XPS spectrum displays the main elements V, O, C and N of the different prepared materials. The observed carbon in VO_2 may be due to the contamination from the precursors used.[60] Similar to the EDX results, the amount of nitrogen in the composites follows the same trend. The moderate value of N might improve the electrochemical results.

Table 2 XPS quantitative analysis of the composition of each sample in atomic percent

	Elements			
Samples	V 2p (at% conc.)	O 1s (at% conc.)	C 1s (at% conc.)	N 1s (at% conc.)
VO_2	37.16	49.81	13.03	—
V@24N-G	40.68	31.31	27.25	0.77
V@48N-G	43.93	34.54	20.52	1.01
V@96N-G	39.62	32.39	26.81	1.18

3.2. Electrochemical performance

3.2.1. V@*X*N-G composites. In order to inspect the electrochemical performance of the as-manufactured V@*X*N-G composite materials, a series of electrochemical tests including cyclic voltammetry (CV), galvanostatic charge/discharge (GCD), electrochemical impedance spectroscopy (EIS), and cycling stability was conducted in three and two-electrode configurations using 0.5 M K_2SO_4 aqueous electrolyte. Fig. 6 exhibits the electrochemical performances of VO_2 and the prepared composites in three-electrode configuration. Fig. 6a displays the CV curves comparing VO_2, N-G and the three composite materials recorded in the potential window range of 0.0–0.8 V *versus* Ag/AgCl using a scan rate of 30 mV s^{-1}. All the samples portrayed a semi-rectangular profile expressing a fast-electrochemical reaction, signifying good electrical conductivity. These shapes also suggest the electrical double layer (EDL) capacitive mechanism.[24] The composite electrode materials reveal a greater CV integrated area compared to the pristine VO_2 and N-G. As illustrated in Fig. 6b, all the electrode materials show GCD curves exhibiting quasi-triangular shapes at a specific current of 0.5 A g^{-1}, which characteristically features the

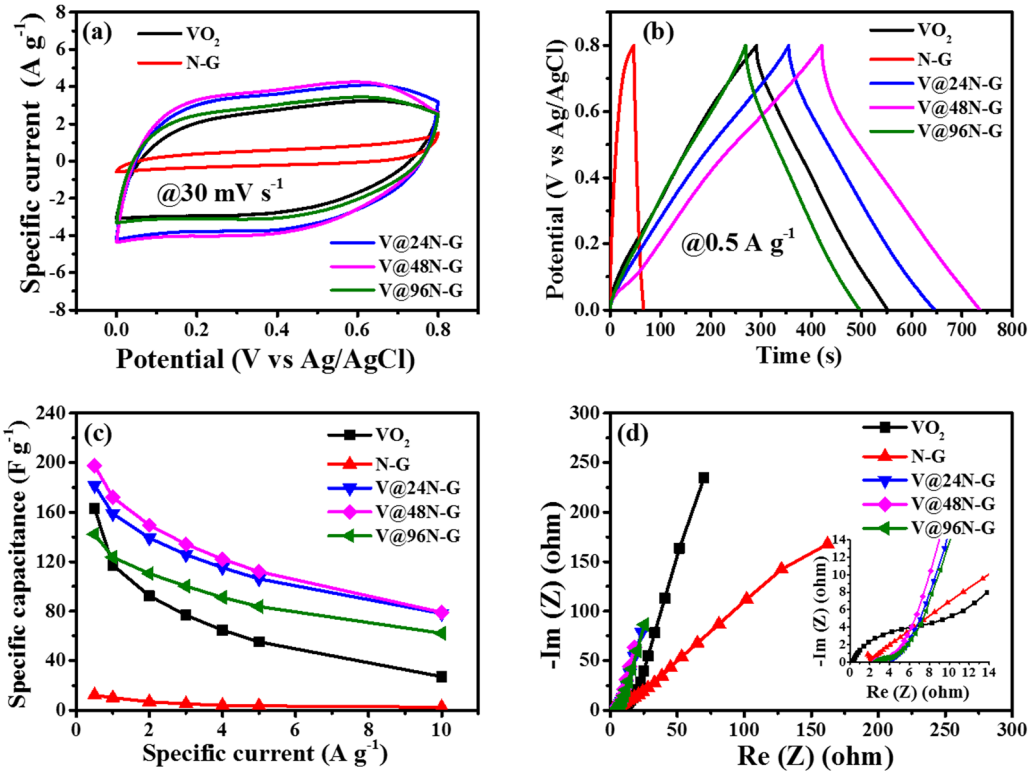

Fig. 6 Comparison of (a) CV at 30 mV s^{-1}, (b) GCD at 0.5 A g^{-1}, (c) C_{sp} *versus* specific current, and (d) Nyquist plot (with an inset at high frequency) of VO_2, N-G and V@*X*N-G.

EDLC and excellent reversibility, confirming the CV in Fig. 6a.[61,62] It is concluded that the GCD of the nanocomposite electrode materials demonstrated the longest discharge time compared to pristine VO_2. However, when the amount of nitrogen was high, a decrease in the discharge time was noticed, as shown in Fig. 6b. The specific capacitances (C_{sp}) were calculated for the different electrode materials, from the GCD using eqn (S1) (ESI†), and plotted *versus* the specific current ranging from 0.5 to 10 A g^{-1}, as presented in Fig. 6c. The attained C_{sp} values at 0.5 A g^{-1} are 163.1 F g^{-1} for VO_2, 12.3 F g^{-1} for N-G; and 181.8, 197.4 and 142.3 F g^{-1} for V@24N-G, V@48N-G and V@96N-G, respectively. We can also conclude here that the composite electrodes performed better, where they showed a good rate capability compared to VO_2 (Fig. 6c). In order to carry out the ions transport dynamic at the interface between the electrode/electrolyte and the conductive properties of the electrodes, EIS was investigated, as shown in Fig. 6(d). Thereby, the charge transfer resistance R_{ct}, estimated at the high frequency region by the diameter of the semicircle, and the solution resistance R_s, representing the point of intersection (first point) between the curve and the real (Re(*Z*)) axis, were figured out. The recorded values in R_s and R_{ct} were (0.4 and 3.8 Ω) for VO_2, (1.8 and 2.3 Ω) for N-G, and (2.7 and 1.4 Ω), (2.5 and 1 Ω) and (2.6 and 1.5 Ω) for V@24N-G, V@48N-G and V@96N-G, respectively. The prepared composite electrodes exhibit a relatively small semicircle, indicating a low R_{ct} at the electrode/electrolyte interface.[63]

In the low-frequency region, they display a diffusion length short and close to the imaginary (Im(*Z*)) axis linked to VO_2 (see Fig. 6d), implying a better capacitive characteristic.[59]

In summary, the V@48N-G composite showed a CV curve displaying a slight larger integrated area, a longer discharge time associated with the superior specific capacitance, and a lower R_s (2.5 Ω) and R_{ct} (1 Ω) compared to the other composite materials. Therefore, this comparison proves that V@48N-G shows inferior electrolyte ions diffusion resistance and R_{ct} and excellent capacitive performance, which are in accordance with the CV and GCD.[61] Thus, the V@48N-G composite electrode outperforms the other composites. This can be attributed to the medium amount of nitrogen added, leading to the good incorporation between VO_2 and N-G materials, as detected in the SEM analysis (Fig. 3c and d). Therefore, a good synergistic effect between VO_2 and N-G can be noted for this particular doping. The better electrochemical results attained with the composite electrodes can be attributed to the synergistic effect due to the presence of effective channels, allowing the passage of charges and ions and also to the great electrical conductivity, good mechanical flexibility and high electrochemical stability arising from the rGO material and the pseudocapacitive behavior from VO_2 and nitrogen-doping.[64]

Moreover, the addition of nitrogen atoms can significantly transform the chemical and electronic properties of the rGO lattice structure, leading to more active sites and improving the wettability through its pseudocapacitive behavior. The good surface wettability at the electrode/K_2SO_4 aqueous electrolyte interface reduces the diffusion resistance between the electrolyte ions and electrode material.[57,65]

Given that for the prepared composite materials, V@48N-G showed superior electrochemical performance, its detailed

measurements were performed firstly in a half-cell (three-electrode) configuration by varying the scan rate, and the specific current for CV and GCD, respectively, in a working potential window from 0.0 to 0.8 V *vs.* Ag/AgCl, by assembling a full-cell device.

Fig. 7 displays further the three-electrode analysis of the V@48N-G composite. Fig. 7a shows the CV profiles at various scan rates values ranging from 5 to 100 mV s^{-1}. They revealed a quasi-rectangular profile, approving the EDL capacitive behavior. From a low (5 mV s^{-1}) to high (100 mV s^{-1}) scan rate, the CV curves maintain a quasi-rectangular shape without any significant distortion, demonstrating the high rate capability of this electrode material.[66] Obviously, the CV curves showed an increase in the current response and integrated area proportional to the scan rate. Fig. 7b relates the analogous GCD at various current densities, showing a linear variation of the charge and discharge path at all the current densities, designating a near-isosceles triangular profile confirming the EDL capacitor behavior seen in Fig. 7a. Fig. 7c displays the electrode's cyclic properties *versus* the cycle number. The electrode showed an excellent Coulombic efficiency of 99.9% and maintained 74.5% of its initial specific capacitance up to 5000 charge and discharge cycles at 10 A g^{-1}. The cycling stability performance of the electrode material (V@48N-G) rapidly decreased after 1500 cycles. This decrease in the stability as a function of cycle number could be related to the formation of the vanadium species such as $HV_2O_7^{3-}$, $V_2O_7^{7-}$, $V_4O_7^{2-}$, or VO_4^{3-} into the electrolyte owing to the over oxidation, which leads to the dissolution of V^{5+} in the oxide phase.[28,67] The dissolution of the vanadium species into the electrolyte during cycling negatively affects the cycling performance, as reported by Shu *et al.*[67] This might explain the immediate decrease in the capacitance retention after 1500 cycles, as observed in Fig. 7c. Thus, the cycling performance is affected by the amount of the vanadium species in the electrolyte, which might be significant after 1500 cycles.

3.2.2. Asymmetric supercapacitor device. To assemble an asymmetric supercapacitor device, cocoa waste-based activated carbon (ACC) adopted from our previous work[29] was examined in 0.5 M K_2SO_4 neutral electrolyte in the three-electrode configuration for a negative electrode (represented in Fig. S5, ESI†). The CV curves (Fig. S5a, ESI†) depict a characteristic rectangular outline, while the GCD curves (Fig. S5b, ESI†) show semi-triangular shapes, indicating the EDL capacitive behavior. The C_{sp} calculated against specific currents is displayed in Fig. S5c (ESI†), indicating a maximum value of 165.6 F g^{-1} at 0.5 A g^{-1}. The Nyquist plot in Fig. S5d (ESI†) shows an equivalent solution resistance (R_s) and charge transfer (R_{ct}) value of 1.8 and 0.3 Ω, respectively.

The asymmetric supercapacitor was made using V@48N-G and ACC as the positive and negative electrode, respectively, in the neutral electrolyte mentioned above. Due to the difference in the specific capacitance of V@48N-G and ACC, a charge balance was carried out ($Q_+ = Q_-$) by calculating the mass of each electrode in the device using eqn (S5) and (S6) (ESI†). The optimal mass ratio between V@48N-G and ACC electrodes was

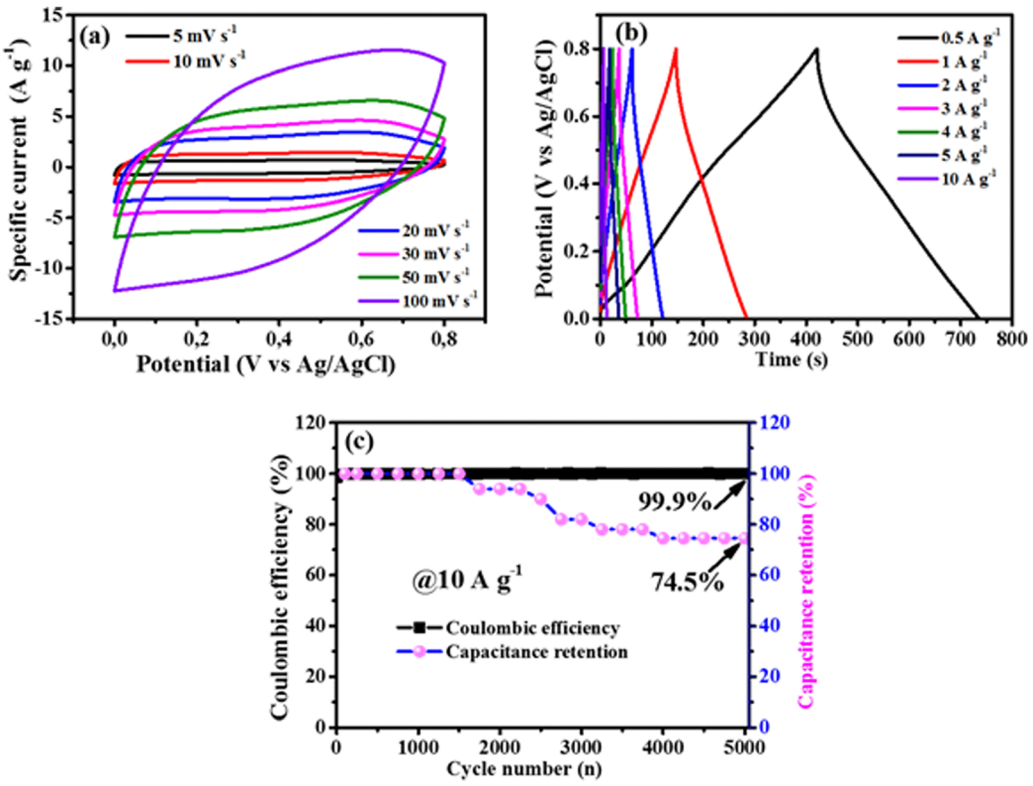

Fig. 7 (a) CV and (b) GCD profiles at different scan rates and specific currents, and (c) cycling stability test of V@48N-G up to 5000 GCD cycles.

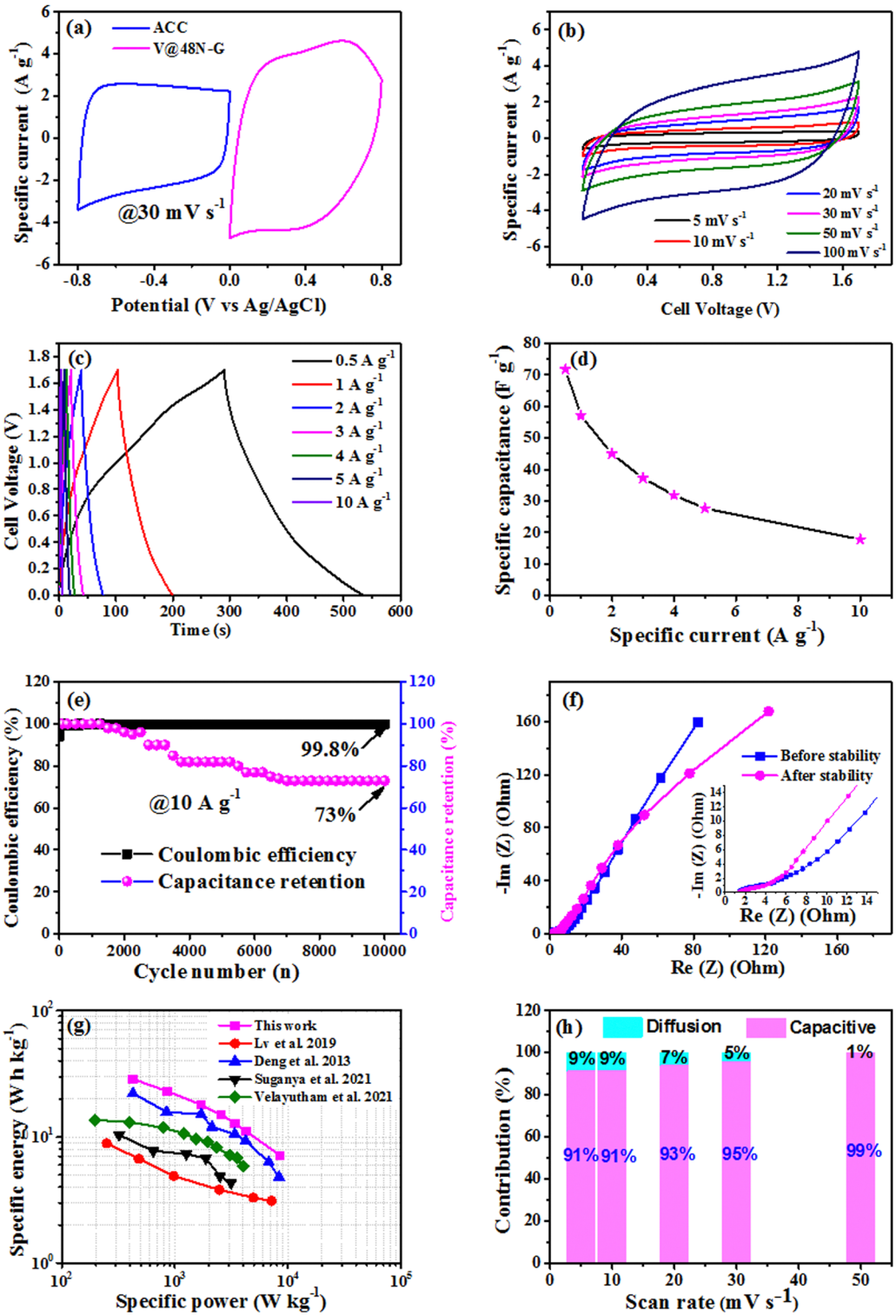

Fig. 8 (a) CV of ACC and V@48N-G examined in the three-electrode set-up in their stable potential window. V@48N-G//ACC device: (b) CV curves, (c) GCD curves, (d) specific capacitance *versus* specific current, (e) Coulombic efficiency and capacitance retention as a function of the cycle number, (f) Nyquist plot studied before and after the stability test, (g) Ragone plots showing a comparison between this work and recently reported results in the literature, and (h) capacitive and diffusion-controlled contributions *vs.* scan rate.

~0.84 in the asymmetric cell. This leads to approximately 2.2 and 1.8 mg as the masses in the negative and positive, respectively, which exhibits in whole 4.0 mg (approximately 2.3 mg cm^{-2}).

Fig. 8a relates the characteristic of the singular CV curves of ACC and V@48N-G composite electrodes tested in the three-electrode configuration, each in its operational potential windows range from −0.8 to 0.0 V and 0.0 to 0.8 V, respectively,

using the same references cited above at 30 mV s^{-1}. Fig. 8b represents the CV profile of the device at diverse sweep rates from 5 to 100 mV s^{-1} within a potential difference of 1.7 volts, revealing an EDLC behavior. From low (5 mV s^{-1}) to high (100 mV s^{-1}) sweep rate, the CV shapes of the device maintained a quasi-rectangular profile, implying its good capacitive behavior, which reveals good ion diffusion and great rate capability.[68,69] Fig. 8c shows the galvanostatic CD of the V@48N-G//ACC device at diverse current densities from 0.5 to 10 A g^{-1}. All galvanostatic CD profiles exhibit semi-triangular shapes, suggesting good double-layer capacitive charge storage in the assembled single-ended supercapacitor, demonstrating the EDLC behavior characteristics of the single-ended device, as confirmed by the CV^2.

To deeply probe the contributions of capacitive and diffusion-controlled behaviors within the assembled asymmetric V@48N-G//ACC device, the CV curves displayed in Fig. 8b were explored to obtain the values of the current response (i) corresponding to the scan rate (ν) using various scan rates, according to the power law ($i = a\nu^b$), where the values a and b are adjustable. Thus, there are two well-characterized values of b, where the b-value of 1 indicates that the current is controlled by the surface-controlled behavior, while the b-value of 0.5 indicates that the current is controlled by diffusion-controlled behavior. The value of b was determined by plotting the logarithm of the current (i) *versus* the logarithm of the scan rate (ν), as displayed in Fig. S6b (ESI†), whose slope represents the b-value at a certain cell voltage. The two values of b were determined at cell voltages of about 0.4 and 1.5 (Fig. S6a, ESI†), revealing b-values of 0.98 and 0.96, respectively. These values are approximately equal and very close to 1, implying the dominance of the capacitive behavior for the asymmetric device.[70,71] Moreover, Trasatti's analysis was performed to estimate the diffusion-controlled and capacitive contributions within the prepared V@48N-G//ACC device using eqn (S7) and (S8) (ESI†). Based on previous works,[71,72] the total capacitance (C_T) was calculated by the aid of Fig. S7a (ESI†) displaying $1/C$ *versus* $\nu^{0.5}$ using eqn (S9) (ESI†), whereas the EDL capacitance (C_{EDL}) is determined from Fig. S7b (ESI†) exhibiting C *versus* $\nu^{-0.5}$ using eqn (S10) (ESI†). The diffusion-controlled (C_{dif}) was estimated from the difference between C_T and C_{EDL}. Consequently, the capacitive and diffusion-controlled contributions were calculated at various scan rates and plotted (Fig. 8h). The results revealed that the capacitive contribution is higher than the diffusion-controlled contribution, as shown in Fig. 8h. Thus, Trasatti's analysis confirms the dominance of the capacitive behavior, as suggested by the power law, *i.e.*, the V@48N-G//ACC is an EDLC-dominated device.

Fig. 8d displays the full-cell specific capacitance (C_d) against specific current, calculated from CD (Fig. 8c) using eqn (S2) (ESI†). The fabricated full-cell presented a high specific capacitance value of 71.8 F g^{-1} at 0.5 A g^{-1}. At this specific current, it displayed a good specific energy of 28.8 W h kg^{-1}, which corresponds to a power density of 425.1 W kg^{-1}, calculated using eqn (S3) and (S4) (ESI†). Overall, the specific energy and power recorded with the V@48N-G//ACC full-cell are greater compared to those described for most reports on vanadium dioxide and other vanadium oxide/carbon-derived composite materials. For instance, Lv *et al.*[24] manufactured free-standing thin vanadium oxide nanobelts and reduced graphene oxide (VO_2/rGO) composite film. The VO_2/rGO composite film and gel organic electrolyte (PVA/LiCl) were used to fabricate a symmetric supercapacitor. The solid-state supercapacitor exhibited an energy density of 8.96 W h kg^{-1} at a power density value of 250 W kg^{-1} [24]. Deng *et al.*[73] prepared a composite material of graphene and VO_2 (RG/VO_2) *via* a hydrothermal approach by the aid of the precursors ammonium vanadate, graphite oxide (GO) and formic acid. The assembled asymmetric supercapacitor (RG/VO_2//RG) used RG and RG/VO_2 as the negative and positive electrodes, respectively, delivered an energy density of 22.8 W h kg^{-1} corresponding to a power density of 425 W kg^{-1} using 0.5 M K_2SO_4 neutral solution and a current density of 0.5 A g^{-1}.[73] Velayutham and co-workers[74] reported the electrodeposition method to attain the binder-free vanadium pentoxide nanostructure on flexible CFC through the chronoamperometry method. The fabricated V_2O_5@CFC-30//O, N, S@AC device displayed energy and power densities of 17.7 W h kg^{-1} and 2728 W kg^{-1} at 1 A g^{-1} in 1 M Na_2SO_4 neutral medium, respectively.[74] Suganya *et al.*[75] reported N-doped graphene-anchored $Zn_3V_2O_8$ composite synthesized by the hydrothermal process ($Zn_3V_2O_8$@graphene). The assembled asymmetric supercapacitor combining the synthesized composite (positive) and activated carbon (AC) (negative) ($Zn_3V_2O_8$@graphene//AC) recorded a specific energy of 10.4 W h kg^{-1} at a specific power of 312.5 W kg^{-1} in 0.5 M K_2SO_4 at 1 A g^{-1}.[75] This comparative study is summarized in Fig. 8g, which displays the so-called Ragone plot exhibiting the specific energy against the specific power.

The better performance arising from the V@48N-G//ACC device is attributed to the nitrogen-doping, where the conductivity of the sample increased owing to the extra lone pair of electrons in nitrogen atoms. This may offer a negative charge density for the sp^2 hybrid carbon skeleton of the delocalized π system, thus facilitating electron transport.[76,77] Also, it enhances the wettability of the electrode materials' surface, which can enable the electrode/electrolyte ion contact.[78]

Furthermore, the electronegativity value of nitrogen atom (3.0) is superior to that of carbon atom (2.5), which leads to positive charge density near the adjacent carbon atoms.[79] This increases the material's polarization, a characteristic representing the EDLC.[80]

To evaluate the stability performance, the device (V@48N-G//ACC) was constrained to 10 000 GCD cycles at 10 A g^{-1}. The cyclic property is a key test for the fabricated full-cell to be considered for practical applications in supercapacitors. Therefore, the plot of both Coulombic efficiency and capacitance retention as a function of cycle number is represented in Fig. 7e. It recorded an important cyclic performance with an excellent Coulombic efficiency of 99.8% and retained 73% of the initial specific capacitance over 10 000 GCD cycles. The decrease in the capacitance retention with the number of charge/discharge cycles can be attributed to the destruction of the nanocomposite materials in the electrode and the mass loss of the electrode after 10 000 charge/discharge cycles.[81]

Fig. 7f shows the Nyquist plots of the asymmetric device before and after stability. At high frequency (inset in Fig. 7f), the device shows equivalent series resistances (R_s) approximately identical and equal to 1.42 Ω before stability and 1.47 Ω after stability. Still, in this region of high frequencies, the inset in Fig. 7f reveals the absence of a semicircle, indicating a very low charge transfer resistance, which results in good ionic conductivity. This favours the rapid formation of the EDL in these electrodes.[82] At low frequency, a short diffusion path length and closeness to the Im(Z) axis is observed, indicating the capacitive behavior of the asymmetric cell.[82] The low R_s attained for this device allowed to obtain an important maximum power device P_{max} of 127.2 kW kg^{-1} estimated from eqn (S11) (ESI†).

The diffusion length faintly increased with a minor deviation from the Im(Z) axis. This is ascribed to a reduction in the ionic conductivity due to a drop of ions in the electrolyte solution after a long galvanostatic charge/discharge cycle. The degradation of the electrode surface (oxidation) after the stability test can similarly lower the ionic conductivity and lead to an increase in the diffusion length.[83]

4. Conclusion

In this study, vanadium dioxide nitrogen-doped rGO composite material (V@*X*N-G) has been effectively prepared utilizing a one-step solvothermal process *via* the variation of the amount of urea (N source) introduced into the rGO matrix. Thus, V@24N-G, V@48N-G and V@96N-G composite samples were obtained. The three-electrode measurements in 0.5 M K_2SO_4 electrolyte illustrated that the optimized sample corresponds to V@48N-G. This sample exhibited a C_{sp} value of 197.4 F g^{-1} at 0.5 A g^{-1} within a large voltage window range of 0.0–0.8 V *vs.* Ag/AgCl. The V@48N-G electrode material recorded an excellent Coulombic efficiency of ~99.9% with a capacitance retention of 74.5% over 5000 GCD cycles at 10 A g^{-1}. An asymmetric full-cell device assembled using V@48N-G positive electrode and ACC negative electrode (V@48N-G//ACC) provided a good specific energy of 28.8 W h kg^{-1}, which corresponds to a specific power of 425.1 W kg^{-1}, recorded at 0.5 A g^{-1} at a large potential difference of 1.7 V. Due to the low equivalent series resistance, the device delivered a great maximum power P_{max} of 127.2 kW kg^{-1}. Moreover, the device showed remarkable cyclic properties with an excellent Coulombic efficiency of 99.8% and a capacitance retention of 73% after 10 000 GCD cycles. These results elucidate that the prepared material has impressive potential for energy storage applications.

Data availability

Data can be available upon request from the authors.

Conflicts of interest

The authors declare that they have no known competing financial interest or personal relationships that could have appeared to influence the work reported in this paper.

Acknowledgements

This work was sponsored by the South African Research Chairs Initiative (SARChI) of the National Research Foundation (NRF) (Grant UID. 61056). Any opinion, finding and conclusion expressed in this work are those of the author(s) and NRF accepts no responsibility in this respect. S. Sarr acknowledges funding from the University of Pretoria and the National Research Foundation-The World Academy of Science (NRF-TWAS) for his doctoral studies. The authors acknowledge Prof Mohamed Chaker laboratory, the National Institute of the Scientific Research (INRS) – Energy Materials Telecommunication Centre (EMT), Canada, Quebec for XPS measurements.

References

1 H. Wang, H. Chen, X. Hou, H. Ye, Z. Guo, Z. Chen, Y. Jin, Y. Du and P. Ren, *Diamond Relat. Mater.*, 2023, **136**, 109888.
2 W. Zhang, R. Guo, L. Dang, J. Sun, Z. Liu and Z. Lei, *J. Power Sources*, 2021, **507**, 230303.
3 S. R. Sinsel, R. L. Riemke and V. H. Hoffmann, *Renewable Energy*, 2020, **145**, 2271–2285.
4 M. K. Sahoo, P. Mane, B. Chakraborty and J. N. Behera, *Inorg. Chem.*, 2024, **63**, 6383–6395.
5 A. S. Lemine, M. M. Zagho, T. M. Altahtamouni and N. Bensalah, *Int. J. Energy Res.*, 2018, **42**, 4284–4300.
6 F. Niu, X. Han, H. Sun, Q. Li, X. He, Z. Liu, J. Sun and Z. Lei, *ACS Sustainable Chem. Eng.*, 2021, **9**, 4146–4156.
7 H. Sun, F. Niu, P. Yuan, X. He, J. Sun, Z. Liu, Q. Li and Z. Lei, *Small Struct.*, 2021, **2**, 1–9.
8 M. J. Madito, K. S. Matshoba, F. U. Ochai-Ejeh, N. Mongwaketsi, C. B. Mtshali, M. Fabiane and N. Manyala, *Surf. Coat. Technol.*, 2020, **383**, 125230.
9 C. Leng, Z. Zhao, Y. Song, L. Sun, Z. Fan, Y. Yang, X. Liu, X. Wang and J. Qiu, *Nano-Micro Lett.*, 2021, **13**, 1–11.
10 A. T. A. Ahmed, H. S. Chavan, Y. Jo, S. Cho, J. Kim, S. M. Pawar, J. L. Gunjakar, A. I. Inamdar, H. Kim and H. Im, *J. Alloys Compd.*, 2017, **724**, 744–751.
11 Y. Wang, Y. Song and Y. Xia, *Chem. Soc. Rev.*, 2016, **45**, 5925–5950.
12 Q. Jiang, N. Kurra, M. Alhabeb, Y. Gogotsi and H. N. Alshareef, *Adv. Energy Mater.*, 2018, **8**, 1–10.
13 W. Guo, C. Yu, S. Li, Z. Wang, J. Yu, H. Huang and J. Qiu, *Nano Energy*, 2019, **57**, 459–472.
14 S. Chen, H. Yu, L. Chen, H. Jiang and C. Li, *Chem. Eng. J.*, 2021, **423**, 130208.
15 R. Basu, S. Ghosh, S. Bera, A. Das and S. Dhara, *Sci. Rep.*, 2019, **9**, 4621.
16 Z. Khan, P. Singh, S. A. Ansari, S. R. Manippady, A. Jaiswal and M. Saxena, *Small*, 2021, **17**, 1–33.
17 M. Guo, J. Balamurugan, T. D. Thanh, N. H. Kim and J. H. Lee, *J. Mater. Chem. A*, 2016, **4**, 17560–17571.
18 W. D. Wang, P. P. Zhang, S. Q. Gao, B. Q. Wang, X. C. Wang, M. Li, F. Liu and J. P. Cheng, *J. Colloid Interface Sci.*, 2020, **579**, 71–81.
19 B. D. Ngom, N. M. Ndiaye, N. F. Sylla, B. K. Mutuma, N. Manyala and M. Chaker, *Philos. Trans. R. Soc., A*, 2021, **379**, 20200347.

20 R. Guo, J. Li, Y. Jia, F. Xin, J. Sun, L. Dang, Z. Liu and Z. Lei, *J. Mater. Chem. A*, 2019, **7**, 4165–4174.
21 L. Liang, H. Liu and W. Yang, *J. Alloys Compd.*, 2013, **559**, 167–173.
22 X. Xiao, S. Li, H. Wei, D. Sun, Y. Wu, G. Jin, F. Wang and Y. Zou, *J. Mater. Sci.: Mater. Electron.*, 2015, **26**, 4226–4233.
23 M. Dhanda, S. P. Nehra and S. Lata, *Synth. Met.*, 2022, **286**, 117046.
24 W. Lv, C. Yang, G. Meng, R. Zhao, A. Han, R. Wang and J. Liu, *Sci. Rep.*, 2019, **9**, 1–8.
25 P. Bharathidasan, S. Devaraj and S. R. Sivakkumar, *J. Solid State Electrochem.*, 2020, **24**, 1095–1103.
26 Z. Liu, D. Li, Z. Li, Z. Liu and Z. Zhang, *Appl. Surf. Sci.*, 2017, **422**, 339–347.
27 S. R. Mangisetti, M. Kamaraj and S. Ramaprabhu, *Electrochim. Acta*, 2019, **305**, 264–277.
28 S. Sarr, N. F. Sylla, D. T. Bakhoum, K. O. Oyedotun, B. D. Ngom and N. Manyala, *J. Energy Storage*, 2021, **43**, 103294.
29 S. Sarr, N. F. Sylla, D. T. Bakhoum, N. M. Ndiaye, D. J. Tarimo, V. M. Maphiri, B. D. Ngom and N. Manyala, *J. Energy Storage*, 2022, **55**, 105666.
30 D. J. Tarimo, K. O. Oyedotun, A. A. Mirghni and N. Manyala, *Int. J. Hydrogen Energy*, 2020, **45**, 13189–13201.
31 A. A. Boochakravarthy, M. Dhanasekar and S. Venkataprasad Bhat, *AIP Adv.*, 2020, **10**, 85127.
32 N. M. Ndiaye, N. F. Sylla, B. D. Ngom, F. Barzegar, D. Momodu and N. Manyala, *Electrochim. Acta*, 2019, **316**, 19–32.
33 S. Li, Y. Cen, Q. Xiang, M. K. Aslam, B. Hu, W. Li, Y. Tang, Q. Yu, Y. Liu and C. Chen, *J. Mater. Chem. A*, 2019, **7**, 1658.
34 N. F. Sylla, N. M. Ndiaye, B. D. Ngom, B. K. Mutuma, D. Momodu, M. Chaker and N. Manyala, *J. Colloid Interface Sci.*, 2020, **569**, 332–345.
35 C. S. Ramirez-Barria, D. M. Fernandes, C. Freire, E. Villaro-Abalos, A. Guerrero-Ruiz and I. Rodríguez-Ramos, *Nanomaterials*, 2019, **9**, 1761.
36 C. M. Chen, Q. Zhang, X. C. Zhao, B. Zhang, Q. Q. Kong, M. G. Yang, Q. H. Yang, M. Z. Wang, Y. G. Yang, R. Schlögl and D. S. Su, *J. Mater. Chem.*, 2012, **22**, 14076–14084.
37 C. M. Masemola, N. Moloto, Z. N. Tetana, S. S. Gqoba, P. K. Mubiayi and E. C. Linganiso, *Mater. Chem. Phys.*, 2022, **287**, 126229.
38 X. Liu, J. Zheng, X. Jing, Y. Cheng and C. Meng, *Appl. Sci.*, 2020, **10**, 2742.
39 A. B. Habtemariam, A. Simo and M. Maaza, *Appl. Phys. A: Mater. Sci. Process.*, 2020, **126**, 1–9.
40 X. Li, S. Zhang, L. Yang, X. Li, J. Chen and C. Huang, *New J. Chem.*, 2017, **41**, 15260–15267.
41 L. Li, Y. Dou, L. Wang, M. Luo and J. Liang, *RSC Adv.*, 2014, **4**, 25658–25665.
42 G. Nie, L. Zhang, J. Lei, L. Yang, Z. Zhang, X. Lu and C. Wang, *J. Mater. Chem. A*, 2014, **2**, 2910–2914.
43 J. Qin, J. Shen, X. Xu, Y. Yuan, G. He and H. Chen, *Microchim. Acta*, 2018, **185**, 459.
44 S. Guan, A. Rougier, M. R. Suchomel, N. Penin, K. Bodiang and M. Gaudon, *Dalton Trans.*, 2019, **48**, 9260–9265.
45 H. C. Youn, S. M. Bak, M. S. Kim, C. Jaye, D. A. Fischer, C. W. Lee, X. Q. Yang, K. C. Roh and K. B. Kim, *ChemSusChem*, 2015, **8**, 1875–1884.
46 S. I. El-Hout, S. G. Mohamed, A. Gaber, S. Y. Attia, A. Shawky and S. M. El-Sheikh, *J. Energy Storage*, 2021, **34**, 102001.
47 M. Mirzaeian, Q. Abbas, D. Gibson and M. Mazur, *Energy*, 2019, **173**, 809–819.
48 J. Jayachandiran, J. Yesuraj, M. Arivanandhan, A. Raja, S. A. Suthanthiraraj, R. Jayavel and D. Nedumaran, *J. Inorg. Organomet. Polym. Mater.*, 2018, **28**, 2046–2055.
49 A. Bordbar-Khiabani, S. Ebrahimi and B. Yarmand, *Appl. Surf. Sci.*, 2019, **486**, 153–165.
50 D. T. Bakhoum, S. Sarr, V. M. Maphiri, N. F. Sylla, N. M. Ndiaye, M. Diop, B. D. Ngom, M. Chaker and N. Manyala, *J. Energy Storage*, 2024, **80**, 110353.
51 M. K. Sahoo, N. Bishoyi, K. Swain and J. N. Behera, *Sustainable Energy Fuels*, 2022, **6**, 4779–4786.
52 S. Li, Y. Cen, Q. Xiang, M. K. Aslam, B. Hu, W. Li, Y. Tang, Q. Yu, Y. Liu and C. Chen, *J. Mater. Chem. A*, 2019, **7**, 1658–1668.
53 D. Mohanadas, N. H. N. Azman and Y. Sulaiman, *J. Energy Storage*, 2022, **48**, 103954.
54 T. A. N. Bui, T. G. Nguyen, W. Darmanto and R. A. Doong, *Electrochim. Acta*, 2020, **361**, 137018.
55 V. N. Kitenge, D. J. Tarimo, G. Rutavi, V. M. Maphiri, S. Sarr, M. Diop, M. Chaker and N. Manyala, *J. Energy Storage*, 2024, **81**, 110453.
56 D. T. Bakhoum, N. F. Sylla, S. Sarr, V. M. Maphiri, N. M. Ndiaye, D. J. Tarimo, A. Seck, B. D. Ngom, M. Chaker and N. Manyala, *J. Energy Storage*, 2023, **68**, 107695.
57 J. Zhao, W. Zhang, X. Guo, Z. Zhang, H. Xie, Y. Zheng, S. Wang, Q. Xu, Q. Fu and T. Zhang, *Mater. Chem. Phys.*, 2022, **287**, 126311.
58 S. Lu, L. Sui, M. Wu, S. Zhu, X. Yong and B. Yang, *Adv. Sci.*, 2019, **6**, 1801192.
59 N. F. Sylla, S. Sarr, N. M. Ndiaye, B. K. Mutuma, A. Seck, B. D. Ngom, M. Chaker and N. Manyala, *Nanomater.*, 2021, **11**, 1056.
60 N. M. Ndiaye, T. M. Masikhwa, B. D. Ngom, M. J. Madito, K. O. Oyedotun, J. K. Dangbegnon and N. Manyala, *Mater. Chem. Phys.*, 2018, **214**, 192–200.
61 D. Gandla, X. Wu, F. Zhang, C. Wu and D. Q. Tan, *ACS Omega*, 2021, **6**, 7615–7625.
62 G. A. Yakaboylu, C. Jiang, T. Yumak, J. W. Zondlo, J. Wang and E. M. Sabolsky, *Renewable Energy*, 2021, **163**, 276–287.
63 L. Wang, S. Li, F. Huang, X. Yu, M. Liu and H. Zhang, *J. Power Sources*, 2019, **439**, 227103.
64 N. M. Ndiaye, B. D. Ngom, N. F. Sylla, T. M. Masikhwa, M. J. Madito, D. Momodu, T. Ntsoane and N. Manyala, *J. Colloid Interface Sci.*, 2018, **532**, 395–406.
65 N. H. A. Rosli, K. S. Lau, T. Winie, S. X. Chin and C. H. Chia, *Diamond Relat. Mater.*, 2021, **120**, 108696.
66 S. Chen, X. Zhou, X. Ma, L. Li, P. Sun and M. Zhang, *RSC Adv.*, 2019, **9**, 30957–30963.
67 D. Shu, H. Cheng, C. Lv, M. A. Asi, L. Long, C. He, X. Zou and Z. Kang, *Int. J. Hydrogen Energy*, 2014, **39**, 16139–16150.

68 J. Du, L. Liu, Z. Hu, Y. Yu, Y. Zhang, S. Hou and A. Chen, *ACS Sustainable Chem. Eng.*, 2018, **6**, 4008–4015.
69 P. Man, Q. Zhang, J. Sun, J. Guo, X. Wang, Z. Zhou, B. He, Q. Li, L. Xie, J. Zhao, C. Li, Q. Li and Y. Yao, *Carbon*, 2018, **139**, 21–28.
70 J. Liu, J. Wang, C. Xu, H. Jiang, C. Li, L. Zhang, J. Lin and Z. X. Shen, *Adv. Sci.*, 2018, **5**, 1700322.
71 V. M. Maphiri, D. T. Bakhoum, S. Sarr, N. F. Sylla, G. Rutavi and N. Manyala, *Nanomaterials*, 2022, **12**, 2211.
72 Y. Xu, C. Huang, A. Hu, Z. Fan, C. Chen, Y. Yang, Q. Tang, C. Jiang and X. Chen, *Appl. Surf. Sci.*, 2021, **563**, 150303.
73 L. Deng, G. Zhang, L. Kang, Z. Lei, C. Liu and Z. H. Liu, *Electrochim. Acta*, 2013, **112**, 448–457.
74 R. Velayutham, R. Manikandan, C. J. Raj, A. M. Kale, C. Kaya, K. Palanisamy and B. C. Kim, *J. Alloys Compd.*, 2021, **863**, 158332.
75 B. Suganya, S. Maruthamuthu, J. Chandrasekaran, B. Saravanakumar, E. Vijayakumar, R. Marnadu, H. E. Ali and T. D. Nguyen, *Surf. Interfaces*, 2021, **24**, 101129.
76 X. Sheng, N. Daems, B. Geboes, M. Kurttepeli, S. Bals, T. Breugelmans, A. Hubin, I. F. J. Vankelecom and P. P. Pescarmona, *Appl. Catal., B*, 2015, **176–177**, 212–224.
77 Y. Gao, Q. Wang, G. Ji, A. Li and J. Niu, *RSC Adv.*, 2021, **11**, 5361–5383.
78 X. Zhang, J. Zhao, X. He, Q. Li, C. Ao, T. Xia, W. Zhang, C. Lu and Y. Deng, *Carbon*, 2018, **127**, 236–244.
79 T. Jiang, Y. Wang, K. Wang, Y. Liang, D. Wu, P. Tsiakaras and S. Song, *Appl. Catal., B*, 2016, **189**, 1–11.
80 M. Duraivel, S. Nagappan, B. Balamuralitharan, S. Selvam, S. N. Karthick, K. Prabakar, C.-S. Ha and H.-J. Kim, *New J. Chem.*, 2018, **42**, 11093.
81 H. Gul, A. U. H. A. Shah, U. Krewer and S. Bilal, *Nanomaterials*, 2020, **10**, 118.
82 Z. J. Han, C. Huang, S. S. Meysami, D. Piche, D. H. Seo, S. Pineda, A. T. Murdock, P. S. Bruce, P. S. Grant and N. Grobert, *Carbon*, 2018, **126**, 305–312.
83 E. Karaca, K. Pekmez and N. Ö. Pekmez, *Electrochim. Acta*, 2018, **273**, 379–391.